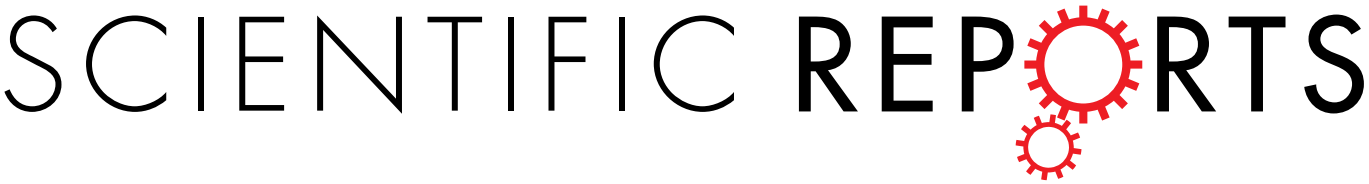

OPEN

Photoluminescence associated with the site occupations of Ho^{3+} ions in $BaTiO_3$

Received: 16 February 2017
Accepted: 14 June 2017
Published online: 21 July 2017

Da-Yong Lu[1,2] & Dong-Xue Guan[3]

A nominal $(Ba_{1-x}Ho_x)Ti_{1-x/4}O_3$ ($x = 0.01$) (BHTH) ceramic with a single-phase tetragonal structure was prepared at 1400 °C using the solid-state reaction method. The analysis on the defect chemistry revealed that the real formula of BHTH is $(Ba_{1-x}Ho_{3x/4})(Ti_{1-x/4}Ho_{x/4})O_3$ with Ba vacancies via electron paramagnetic resonance (EPR). Photoluminescence (PL) was investigated on the basis of excitation with different wavelength lasers. The results indicated that under 488-nm excitation, PL and Raman scattering can occur simultaneously as two distinct optical processes for BHTH ceramic powders, and the strongest PL band at 564 nm was discovered and verified to originate from the $^5G_6/^5F_1 \rightarrow {}^5I_7$ transition of Ho^{3+} ions on the Ti sites in the $BaTiO_3$ lattice. Upon 532- and 638-nm excitations, three PL bands of $^5F_4/^5S_2 \rightarrow {}^5I_8$, $^5F_5 \rightarrow {}^5I_8$, and $^5F_4/^5S_2 \rightarrow {}^5I_7$ transitions are attributed to the contributions from Ho^{3+} ions on the Ba sites. The common Raman spectrum of $BaTiO_3$ can be observed without PL disturbance using 785-nm excitation wavelength. The PL effect may provide a probe for the site occupations of Ho^{3+} ions in widely-used $BaTiO_3$ dielectric ceramics co-doped with Ho^{3+} and other dopants.

Ho^{3+}, as a co-dopant with other dopants (Er^{3+}, Tm^{3+}, Yb^{3+}, Dy^{3+}) in compounds, is widely used in upconversion luminescence in the filed of luminescence[1–6] and in multilayer ceramic capacitors (MLCC) in the filed of dielectrics[7,8]. Barium titanate ($BaTiO_3$) is a typical dielectric material. The dielectric properties and structural information of Ho-doped $BaTiO_3$ were systematically investigated in terms of structural modification[9–15]. Ho^{3+} is known to be an amphoteric dopant in $BaTiO_3$ polycrystalline ceramic and its solid solubility is dependent on the Ba/Ti ratio and sintering temperature (T_s). In the Ti-rich case, Ho^{3+} was considered to to occupy the Ba site to induce Ti vacancies and the solid solubility limit was relatively small, only $x = \sim 1.4\%$ at $T_s = 1400$ °C; the formula was described as $(Ba_{1-x}Ho_x)Ti_{1-x/4}O_3$[10]. Higher T_s is generally required for the incorporation of Ho^{3+} into the Ti site because of a relatively larger ionic size of Ho^{3+} compared to Ti^{4+} (Table 1)[16] and TiO_6 octahedrons characteristic of the skeleton of the perovskite structure. In the Ba-rich case, the solubility limit was reported to be $x = \sim 15\%$ at $T_s = 1550$ °C and the formula was described as $Ba(Ti_{1-x}Ho_x)O_{3-x/2}$ with O vacancies[10,14,15]. However, Ti vacancies and O ones had not been confirmed in Ho-doped $BaTiO_3$ and one is hard to avoid questioning a single site-occupation mode due to the amphoteric nature of Ho^{3+}.

On the other hand, the structural information of $BaTiO_3$ doped with most rare earths such as La[17–20], Ce[21,22], Pr[23], Nd[24], Eu[25], Tb[26], Dy[27], Er[28], Yb[29,30], has been reported via laser Raman spectroscopy to date. However, no Raman information is known about Ho-doped $BaTiO_3$. Because Ho usually acts as a well luminescent center in different host lattices[31–34], the lack of Raman information about Ho-doped $BaTiO_3$ is probably because the preference of strong photoluminescence (PL) caused by Ho^{3+} affects observation of Raman spectra, similar to Er^{3+}[28]. As far as we know, only Battisha[35] and Secu *et al.*[36] reported the up-conversion luminescence (under 808-nm excitation) and PL (under 455-nm excitation) of Ho-doped $BaTiO_3$. Some luminescence bands at 435 ($^5F_1 \rightarrow {}^5I_8$), 545 ($^5F_4, {}^5S_2 \rightarrow {}^5I_8$), 660 ($^5F_5 \rightarrow {}^5I_8$), and 760 nm ($^5F_4, {}^5S_2 \rightarrow {}^5I_7$) were observed. Unfortunately, XRD data show that their Ho-doped $BaTiO_3$ samples prepared at $T_s = 750$ and 1350 °C are not single-phase, accompanied by a secondary phase such as $Ho_2Ti_2O_7$[35,36]. For this reason, the PL origin associated with the site occupations of Ho^{3+}

[1]Research Center for Materials Science and Engineering, Jilin Institute of Chemical Technology, Jilin, 132022, P. R. China. [2]Key Laboratory of Special Functional Materials in Jilin Provincial Universities, Jilin, 132022, P. R. China. [3]College of Chemistry and Pharmaceutical Engineering, Jilin Institute of Chemical Technology, Jilin, 132022, P. R. China. Da-Yong Lu and Dong-Xue Guan contributed equally to this work. Correspondence and requests for materials should be addressed to D.-Y.L. (email: dylu@jlict.edu.cn)

Ion	CN	r (Å)	Ion	CN	r (Å)
Ba^{2+}	12	1.61	Ho^{3+}	12	1.18
Ti^{4+}	6	0.605	Ho^{3+}	6	0.90

Table 1. Ionic radii as a function of coordinate number (CN)[16].

ions in $BaTiO_3$ is still an unresolved scientific problem. Moreover, a distinct exhibition between PL and Raman scattering needs to be also clarified.

In this work, a nominal $(Ba_{1-x}Ho_x)Ti_{1-x/4}O_3$ ($x = 0.01$) ceramic was prepared at 1400 °C using the solid-state reaction method. The defect chemistry is discussed. On the basis of excitation with different wavelength lasers (488–785 nm), photoluminescence and Raman scattering can occur simultaneously as two distinct optical processes for BHTH ceramic powders. The reasonable laser wavelength is indicated for observation for the common Raman phonon modes of Ho-doped $BaTiO_3$. A rare non-ground-state transition corresponding to $^5G_6/^5F_1 \rightarrow {}^5I_7$ of Ho^{3+} was discovered and associated with the site occupations of Ho^{3+} ions in $BaTiO_3$, which may provide a probe for the site occupations of Ho^{3+} ions in $BaTiO_3$-based dielectric ceramics.

Experimental

The initial materials were analytical-reagent chemicals of $BaCO_3$, TiO_2, and Ho_2O_3 (99.9%). Ho-doped $BaTiO_3$ ceramics were prepared using the solid-state reaction method according to the nominal formula $(Ba_{1-x}Ho_x)Ti_{1-x/4}O_3$ ($x = 0.01$) named as BHTH. The weighed powders were dry-mixed and ground. Then, the powders were calcined at 1100 °C for 5 h to decarbonate. The calcined powders were mixed with a small amount of PVA aqueous solution and pressed at a pressure of 200 MPa into pellets (Φ12 mm). These pellets were sintered at $T_s = 1400$ °C for 12 h, and cooled at a cooling rate of −200 °C/h from 1400 °C to 700 °C and then furnace-cooled to room temperature. The pellets were densified into crack-free ceramics. In addition, a nominal $(Ba_{1-x}Ho_x)Ti_{1-x/4}O_3$ ($x = 0.01$) (BH1T) ceramic was prepared at $T_s = 1300$ °C for 12 h for analysis on site-occupation-related photoluminescence of Ho^{3+} ions in the $BaTiO_3$ lattice.

Powder X-ray diffraction (XRD) data were recorded from 20° to 85° and in steps of 0.02° using a DX-2700 X-ray diffractometer (Dandong Haoyuan) at room temperature. Lattice parameters were calculated with MS Modeling (Accelry Inc.) using Cu $K\alpha_1$ radiation ($\lambda = 1.540562$ Å). Microstructure was observed using an EVOMA 10 scanning electron microscope (Zeiss) operated at 15 keV. Photoluminescence (PL) and Raman spectra of the ceramic powders were recorded using a LabRAM XploRA Raman spectrometer (Horiba Jobin Yvon) with 532- (green) and 638-nm (red) lasers and an inVia Raman spectrometer (Renishaw) equipped with 488- (blue-purple) and 785-nm (red) lasers. The laser power level was adjusted to 0.1–10% (Filter) of the normal output of 25 mW because of a huge difference in spectral intensity. The accumulation time and resolution are 2 s and 2.7 cm^{-1}, respectively. Electron paramagnetic resonance (EPR) measurements were performed at room temperature using an EMX Plus X-band spectrometer (Bruker) operating at 9.84 GHz. The gyromagnetic factor (g) was calculated by the relationship $h\nu_0 = g\beta H$, where h is the Planck constant ($h = 6.626 \times 10^{-34}$ J·s), ν_0 is the microwave frequency, β is the Bohr magnetron ($\beta = 9.262 \times 10^{-24}$ J/T), H is the magnetic field strength.

Results and Discussion

Crystal structure, site occupation and microstructure. Figure 1a shows the XRD pattern of $(Ba_{1-x}Ho_x)Ti_{1-x/4}O_3$ ($x = 0.01$) ceramic (BHTH) prepared at $T_s = 1400$ °C. BHTH has a single-phase tetragonal perovskite structure, indicating that Ho^{3+} ions are incorporated sufficiently into the perovskite lattice. This result is in accord with the solubility limit of $x = 0.014$ for $(Ba_{1-x}Ho_x)Ti_{1-x/4}O_3$ at $T_s = 1400$ °C reported by Makovec *et al.*[10].

The lattice parameters (a, c) and unit cell volume (V_0) is shown in Fig. 1a. It is inferred that the expansion in V_0 caused by the occupations of the Ti^{4+} sites by Ho^{3+} ions should be greater than the contraction in V_0 caused by the occupations of the Ba^{2+} sites by Ho^{3+} ions on the basis of the BO_6 octahedrons skeleton characteristic of the perovskite lattice and ionic size comparisons between 12-CN Ba^{2+} and Ho^{3+} and between 6-CN Ti^{4+} and Ho^{3+} (Table 1). The V_0 of BHTH (64.44 $Å^3$) is slightly greater than that of the tetragonal $BaTiO_3$ ($V_{0\text{-BT}} = 64.41$ $Å^3$) (JCPDS Cards No. 6–526), implying that Ho^{3+} ions enter the Ti sites in part except for some Ho^{3+} ions on the Ba sites.

Figure 1b shows the EPR spectrum of BHTH. Ho^{3+} ($4f^{10}$) is a non-Kramers ion, which is EPR silent in theory. A very strong EPR signal at $g = 1.974$ appears in BHTH and was observed in Dy- and Er-doped $BaTiO_3$[27,28]. This signal is assigned to ionized Ba-vacancy defects (V_{Ba})[27,28,37,38]. A $g = 2.004$ signal associated with Ti vacancies is absent for BHTH, revealing that Ti-vacancy defects cannot be formed in the nominal $(Ba_{1-x}Ho_x)Ti_{1-x/4}O_3$ (BHTH) with deliberately designed Ti vacancies; Ho^{3+} ions transfer from the Ba sites to the Ti ones and results in appearance of Ba vacancies in BHTH. This result is in good agreement with the previous XRD result.

Figure 1c and d shows the SEM images on the surface and the interior of BHTH. The surface of the ceramic sintered exhibits an inhomogeneous microstructure (Fig. 1c) with grains (2–20 μm), but the interior in the ceramic shows a fine-grained feature (2–6 μm) (Fig. 1d). This illustrates that the grain growth on the surface is faster than the interior.

Defect chemistry. For the nominal $(Ba_{1-x}Ho_x)Ti_{1-x/4}O_3$ ($x = 0.01$) ceramic (BHTH) sintered at $T_s = 1400$ °C, the above XRD result gives evidence of a single-phase perovskite ceramic and the partial occupations of the Ti sites by Ho^{3+} ions (Fig. 1a); the EPR result reveals that Ti vacancies in BHTH are completely filled by Ho^{3+} and the transfer of Ho^{3+} ions from the Ba sites to the Ti ones gives rise to the presence of Ba vacancies (Fig. 1b). It is obvious that the formula cannot be described as $(Ba_{1-x}Ho_x)Ti_{1-x/4}O_3$ with Ti vacancies suggested by Makovec *et al.*[10]. Ho^{3+} is known to show an amphoteric behavior, substituting for both Ba and Ti sites in $BaTiO_3$[10–12]. Thus, the

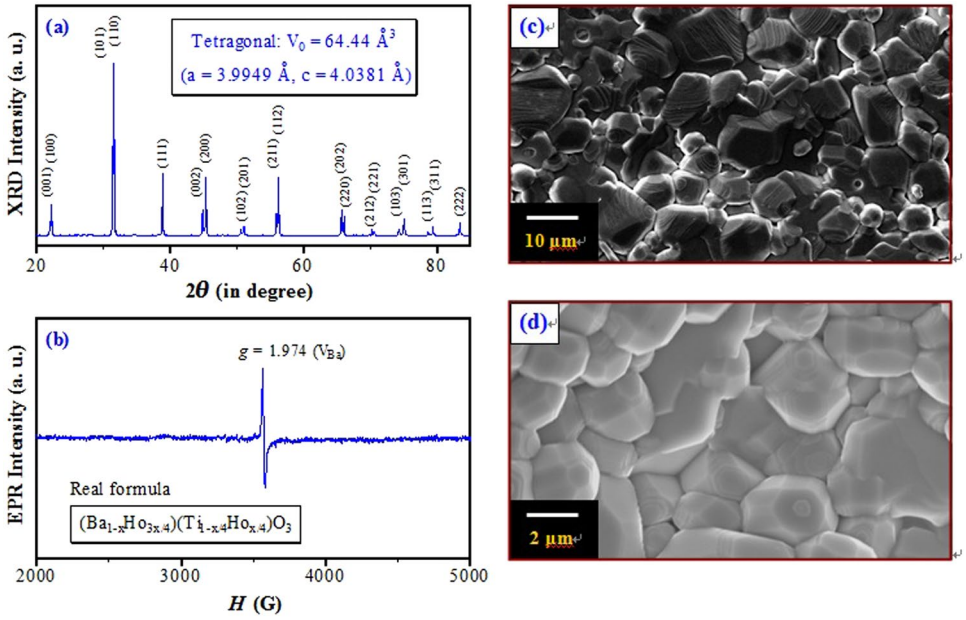

Figure 1. (**a**) XRD pattern, (**b**) EPR spectrum, SEM images on (**c**) the surface and (**d**) the interior for the nominal $(Ba_{1-x}Ho_x)Ti_{1-x/4}O_3$ ($x = 0.01$) ceramic (BHTH) sintered at a sintering temperature of $T_s = 1400\,°C$. The real formula of BHTH is expressed by $(Ba_{1-x}Ho_{3x/4})(Ti_{1-x/4}Ho_{x/4})O_3$ with Ba vacancies (V_{Ba}).

defects in BHTH are Ba-site Ho^{3+} ($Ho^{\bullet}_{Ba}$), Ba vacancies (V''_{Ba}), and Ti-site Ho^{3+} (Ho'_{Ti}). The defect notation adopts that suggested by Kröger and Vink[39]. The lattice electroneutrality is collectively compensated by these three types of point defects. The detailed process of point defects formation is as follows:

Ho^{3+} ions enter both Ba and Ti sites simultaneously, forming the self-compensated $Ho^{\bullet}_{Ba} - Ho'_{Ti}$ defect complexes, similar to $Dy^{\bullet}_{Ba} - Dy'_{Ti}$ [27] and $Er^{\bullet}_{Ba} - Er'_{Ti}$ [28].

$$Ho_2O_3 \rightarrow Ho^{\bullet}_{Ba} + Ho'_{Ti} + 3O_O \quad (1)$$

The partial occupations of the Ti sites by Ho^{3+} ions result in a Ti-rich case. Accordingly, Ba vacancies are induced by the extra Ba-site Ho^{3+} ions excluding $Ho^{\bullet}_{Ba} - Ho'_{Ti}$ to meet the requirement of the lattice electroneutrality.

$$Ho_2O_3 + 3TiO_2 \rightarrow 2Ho^{\bullet}_{Ba} + V''_{Ba} + 3Ti_{Ti} + 9O_O \quad (2)$$

Thus, a very strong EPR signal at $g = 1.974$ is present in BHTH (Fig. 1b). The real formula of BHTH is determined to be $(Ba_{1-x}Ho_{3x/4})(Ti_{1-x/4}Ho_{x/4})O_3$ with double-site substitutions and Ba-vacancy compensation, i.e., that at the doping level of $x = 0.01$, 0.75 at.% Ho^{3+} ions are substituted on the Ba sites and 0.25 at.% Ho^{3+} ions on the Ti sites. The quantitative information on the site occupations of Ho^{3+} ions in BHTH can be drawn from the EPR and XRD results. The defect chemistry of BHTH is the same as that of $BaTiO_3$ doped with Dy[27] and Er[28]. An interesting phenomenon is that Ho (AN = 67) is between Dy (66) and Er (68) in atomic number (AN).

Photoluminescence and Raman spectra. Figure 2a–c show the photoluminescence (PL) spectra of BHTH upon excitations with 638-, 532-, and 488-nm laser lines. Energy level diagram for Ho^{3+} ions in BHTH is shown in Fig. 2d. In the detectable range, these PL bands originate from the 4f-4f inner-shell emission of Ho^{3+} in $BaTiO_3$. Upon 638-nm excitation, Ho^{3+} ions are excited through one-photon absorption from $^5I_8$ to $^5F_5$; the strongest emission band at 653 nm (Fig. 2a) is caused by the $^5F_5 \rightarrow {}^5I_8$ transition. The near infrared (NIR) emission band (755 nm) associated with the $^5F_4/^5S_2 \rightarrow {}^5I_7$ transition might originate from the following process: Ho^{3+} ions are excited through one-photon absorption from the ground state $^5I_8$ to the excited state $^5F_5$ that relaxes nonradiatively to the lying excited state $^5I_7$ *via* continuous multi-phonon relaxation processes ($^5F_5$-$^5I_4$-$^5I_5$-$^5I_6$-$^5I_7$). Subsequently, Ho^{3+} ions were excited again through one-photon absorption (excited state absorption (ESA) process or energy transfer (ET) process) from $^5I_7$ to the excited state $^5F_3$ that relaxes nonradiatively to the emitting level $^5F_4/^5S_2$. Finally, the $^5F_4/^5S_2 \rightarrow {}^5I_7$ transition occurs (Fig. 2d). Each emission band shows a multiplet feature because of the Stark components of the ground state $^5I_8$ and the excited states $^5F_4/^5S_2$ and $^5F_5$[5,31,32,35].

Upon 532-nm excitation, three PL bands with different intensities can be observed (Fig. 2b). The emission mechanism of Ho^{3+} in BHTH does not go through two-step ESA or ET process, but one-step one-photon absorption from $^5I_8$ to $^5F_4/^5S_2$ that relax nonradiatively to the emitting level $^5F_5$, which is the reason that the intensity of the NIR (755 nm) emission band under 532-nm excitation is higher than that under 638-nm excitation. BHTH exhibits strong green (545 nm) with weak red (653 nm) and NIR (755 nm) emission bands associated with $^5F_4/^5S_2 \rightarrow {}^5I_8$, $^5F_5 \rightarrow {}^5I_8$ and $^5F_4/^5S_2 \rightarrow {}^5I_7$ transitions, respectively, of Ho^{3+} ions[31,32]. The multiplet feature of

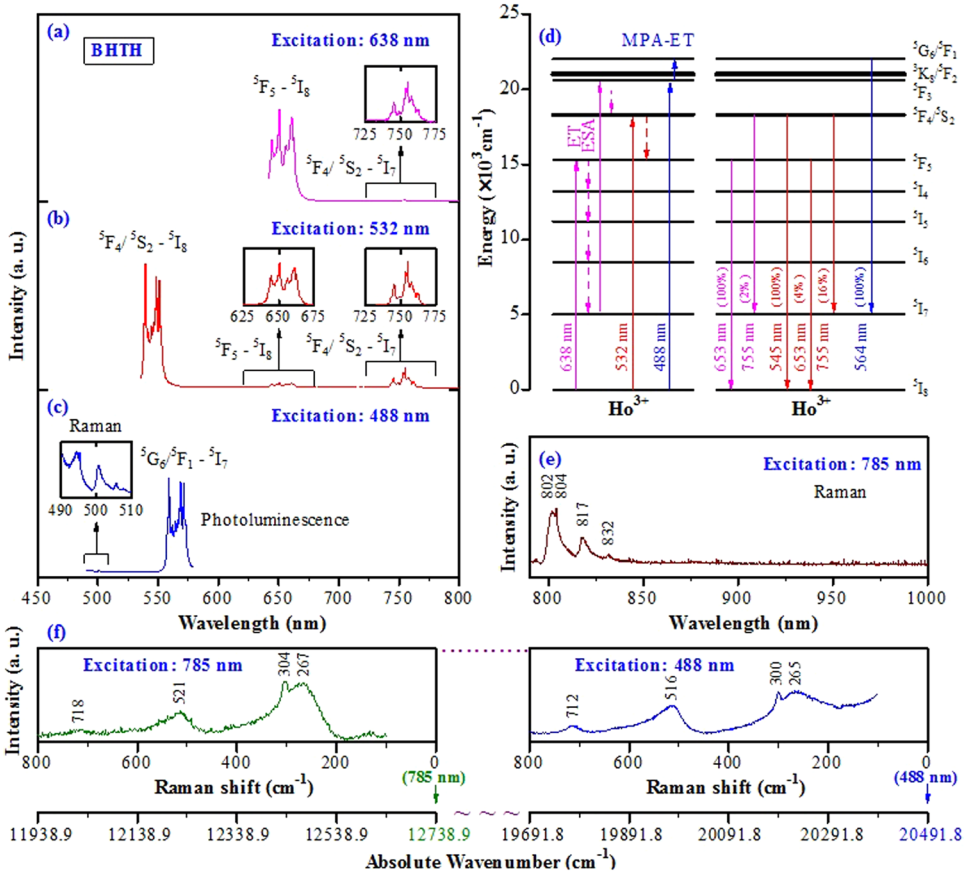

Figure 2. PL spectra of BHTH at room temperature, excitation with (**a**) 638-, (**b**) 532-, and (**c**) 488-nm laser lines. (**d**) Energy level diagram for Ho^{3+} ions in BHTH. MPA-ET represents multi-phonon assisted energy transfer. The values in bracket represent the percentage of the line intensity to the strongest emission line intensity. (**e**) Pure Raman spectrum is observed using 785-nm excitation wavelength. (**f**) Comparison of Raman spectra (stokes components) under 785- and 488-nm excitation wavelengths, shown in Raman shift and absolute wavenumber. The right figure shows the weak bands at around 500 nm in Fig. 2c inset.

bands is also caused by Stark splitting of the energy levels. It can be seen from the insets in Fig. 2a and b that the corresponding emission bands upon excitation with different wavelengths exhibit the same spectral structure.

Pure Raman spectrum was observed in BHTH using 785-nm excitation wavelength, as shown in Fig. 2f. This spectrum of BHTH, which does not show any emission transition line and is similar to that reported for the tetragonal $BaTiO_3$[28,40–42], shows four common bands, with peaks at 267 [A_1 (TO_2)], 304 [$B_1 + E(TO_3 + LO_2)$], 521 [A_1 (TO_3)], and 718 cm^{-1} [A_1 (LO_3) + E (LO_4)], corresponding to 802, 804, 817, and 832 nm in wavelength (Fig. 2e), respectively. No signal was present in the range of 850–1000 nm.

Upon 488-nm excitation, two bands were observed and the intensity of the main PL band at around 564 nm is 40 times that of the weak band at around 500 nm (Fig. 2c). The band at 564 nm, which has not been reported for Ho-doped $BaTiO_3$[31,32], was observed for BHTH (Fig. 2c). This band is attributed to the $^5G_6/^5F_1 \rightarrow {}^5I_7$ transition (Fig. 2d). The following analyses give its emission mechanism, and indicate that the band at 564 nm is associated with Ho^{3+} ions on the Ti sites and the weak band at 500 nm originates from Raman scattering of BHTH.

It is well known that when the excitation is changed to a different wavelength, the Raman bands shift the same amount correspondingly, while the PL lines stay on the same absolute wavenumber[28,43]. Upon 638- and 532-nm excitations, it can be seen that both $^5F_5 \rightarrow {}^5I_8$ and $^5F_4/^5S_2 \rightarrow {}^5I_7$ transition bands at around 653 and 755 nm (Fig. 2a and b) stay on the same position, respectively, illustrating the PL nature of these two bands. Upon 488-nm (20491.8 cm^{-1}) and 785-nm (12738.9 cm^{-1}) excitations, Raman band is easy to be identified by comparison of band positions. Figure 2f shows their spectra, in which the right figure shows the weak band at 500 nm in Fig. 2c inset. When the excitation is changed from 488 nm to 785 nm, the shift of 7752.9 cm^{-1} between two Raman signals was observed for BHTH. Moreover, both spectra exhibit the nearly same spectral structure as the tetragonal $BaTiO_3$ (Fig. 2f). Thus, the band at around 500 nm is confirmed to originate from Raman scattering in the case of excitation at 488 nm.

The $^5G_6/^5F_1 \rightarrow {}^5I_7$ transition most likely originates from ground state absorption plus phonon-assisted transition (Fig. 2d). The $^5F_3$ energy level can be populated from $^5I_8$ via 488-nm laser energy absorption (one-photon). As the energy differences between $^5F_3$ and $^3K_8/^5F_2$ and between $^3K_8/^5F_2$ and $^5G_6/^5F_1$ is about 250 and 1050 cm^{-1}, respectively, the multi-phonon assisted energy transfer (MPA-ET) corresponding to one A_1 (TO_2)

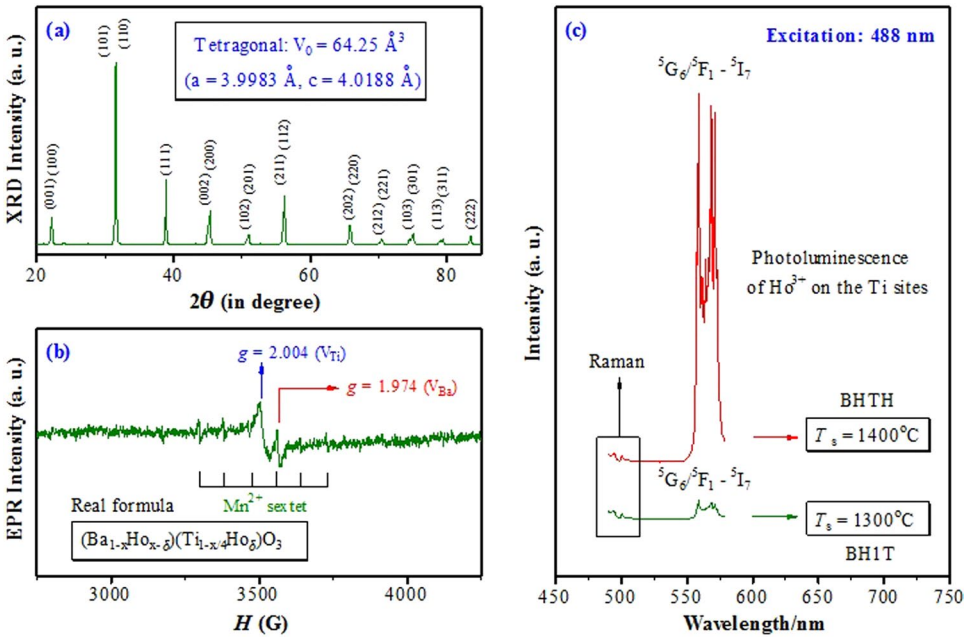

Figure 3. (**a**) XRD pattern, (**b**) EPR spectrum for the nominal $(Ba_{1-x}Ho_x)Ti_{1-x/4}O_3$ ($x = 0.01$) ceramic (BH1T) sintered at $T_s = 1300$ °C. The real formula of BH1T is approximately expressed by $(Ba_{1-x}Ho_{x-\delta})(Ti_{1-x/4}Ho_{\delta})O_3$ (δ is a small quantity) with a small number of Ti-site Ho^{3+} ions. (**c**) The comparison in photoluminescence spectra between BHTH and BH1T clearly reveals that Ti-site Ho^{3+} ions are responsible for $^5G_6/^5F_1 \rightarrow {}^5I_7$ transition of Ho^{3+}.

phonon absorption ($^5F_3 \rightarrow {}^3K_8/^5F_2$) and then two A_1 (TO_3) phonons absorption ($^3K_8/^5F_2 \rightarrow {}^5G_6/^5F_1$) can occur. The absorbed phonons can be detected in light of the Raman spectrum in Fig. 2c inset or Fig. 2f. Normally, the three-phonon absorption is enough for the energy gap between $^5F_3$ and $^5G_6/^5F_1$. Finally, the emission band at 564 nm is due to the transition from $^5G_6/^5F_1$ to the second ground state level $^5I_7$.

On the basis of the above analyses, an important finding is that PL and Raman scattering under 488-nm excitation can occur simultaneously as two distinct optical processes for BHTH ceramic powders. One can also see that the PL signals from the $^5F_4/^5S_2 \rightarrow {}^5I_8$ transition under 532-nm excitation are so intense that they overwhelm the traditional Raman spectra of $BaTiO_3$ (Fig. 2b and Fig. 2c inset). The option for laser wavelength is an important factor in observation of Raman signals.

Photoluminescent origin associated with site occupations of Ho^{3+} in $BaTiO_3$. To investigate the PL origin associated with the site occupations of Ho^{3+} ions in the host $BaTiO_3$ lattice, a $BaTiO_3$ ceramic doped with Ho^{3+} on the Ba site is required to be prepared. In the Ti-rich case of Ba/Ti < 1, Ho^{3+} was considered to enter the Ba site for $(Ba_{1-x}Ho_x)TiO_3$ sintered at $T_s = 1320$–1360°C in air[12–14]. For this reason, we prepared a nominal $(Ba_{1-x}Ho_x)Ti_{1-x/4}O_3$ ($x = 0.01$) ceramic (BH1T) sintered at $T_s = 1300$ °C. BHTH and BH1T have the same stoichiometric proportions in components.

The XRD pattern and EPR spectrum of BH1T as well as a comparison in PL spectra between BHTH and BH1T under 488-nm excitation are shown in Fig. 3. BH1T also exhibits a single-phase tetragonal perovskite structure (Fig. 3a) like BHTH, implying a complete incorporation of Ho^{3+} ions into the host $BaTiO_3$ lattice. The V_0 of BH1T (64.25 Å^3) is less than those of BHTH (64.44 Å^3) and the tetragonal $BaTiO_3$ (64.41 Å^3), suggesting that Ho^{3+} ions are dominantly substituted for the Ba sites.

The EPR monitoring for BH1T shows coexistence of both Ba vacancies and Ti ones, marked by two signals at $g = 1.974$ and 2.004, respectively (Fig. 3b), implying that Ho^{3+} may transfer mutually between the Ba site and the Ti one during ceramic sintering and cooling. This behavior is similar to that of Lu^{3+}-doped $BaTiO_3$[44]. In this case more Ho^{3+} ions in BH1T can be present on the Ba^{2+} sites relative to BHTH, resulting in a stronger donor effect. The Mn^{2+} sextet signal is therefore caused by the reduction of Mn^{4+}/Mn^{3+} to Mn^{2+} impurities in BH1T[45,46].

For Ho-doped $BaTiO_3$ ceramics prepared by Battisha and Secu *et al.*, Ho^{3+} is mainly substituted for the Ba sites because of a lower sintering temperature. They observed some luminescence bands at 435 ($^5F_1 \rightarrow {}^5I_8$), 545 ($^5F_4/^5S_2 \rightarrow {}^5I_8$), 660 ($^5F_5 \rightarrow {}^5I_8$), and 760 nm ($^5F_4/^5S_2 \rightarrow {}^5I_7$)[35,36]. The solid solubility limit of Ho^{3+} ions on the Ba sites is less than $x = \sim 1.4\%$ at $T_s = 1400$ °C[10]. For our BHTH, 0.75 at.% Ho^{3+} ions are substituted on the Ba sites. Thus, the PL bands at 545, 653, and 755 nm (Fig. 2a and b) are attributed to Ho^{3+} ions on the Ba sites.

In a detectable wavelength range, one can see that both PL bands at around 564 nm are nearly the same in spectral structure and different in intensity for BHTH and BH1T, while there is no difference between both Raman bands in a lower-wavelength range at around 500 nm (Fig. 3c). It is obvious that the PL band at around 564 nm does not relate to Ho^{3+} ions on the Ba sites. The above XRD and EPR results reveal that Ho^{3+} ions in

BH1T are dominantly substituted for the Ba sites, which is in good agreement with the site occupations of Ho^{3+} at a lower sintering temperature of $T_s = 1320–1360°C$ in air[12–14]. Similar to the doping behavior of Dy^{3+} or Er^{3+} in $BaTiO_3$[27,28], a small number of Ho^{3+} ions in BH1T inevitably enter the Ti sites. For our BHTH, 0.25 at.% Ho^{3+} ions are substituted on the Ti sites. The PL intensity is proportional to the concentration of Ho^{3+} ions. The PL intensity of the $^5G_6/^5F_1 \rightarrow {}^5I_7$ transition of BH1T is one-twentieth of BHTH (Fig. 3c), which matches the concentration of Ho^{3+} ions on the Ti sites in BH1T and BHTH. Thus, Ho^{3+} ions on the Ti sites are responsible for the $^5G_6/^5F_1 \rightarrow {}^5I_7$ transition at around 564 nm.

It is inferred from the PL intensity that 0.0125 at.% Ho^{3+} ions are substituted on the Ti sites in BH1T, though no quantitative information on the site occupations of Ho^{3+} ions on the Ti sites or Ba ones can be drawn directly from the EPR and XRD results. The real formula of BH1T may be approximately described as $(Ba_{1-x}Ho_{x-\delta})(Ti_{1-x/4}Ho_{\delta})O_3$ (δ is a small quantity, $\delta = 0.0125\%$) with Ba vacancies and Ti ones. Hence, the change in local environment and crystal field at which Ho^{3+} lies plays a decisive role in PL.

PL band at 564 nm as a probe for dielectrics in MLCC. Temperature-stable dielectric materials in MLCC often adopt the core-shell structured $BaTiO_3$ ceramics, in which a fine grain consists of a tetragonal $BaTiO_3$ core and a cubic surface layer consisting of Ho_2O_3 and other oxide, such as Ho/Mg[7,47], Ho/Mn[48], Ho/Zr,[49,50] Ho/Dy[8] etc. The incorporation of additives ions into $BaTiO_3$ particles will reduce dielectric permittivity and dielectric-temperature stability. The sintering process plays an important role in controlling incorporation of Ho^{3+} into $BaTiO_3$ particles. Although at a high sintering temperature (e.g. $T_s = 1550\,°C$[10,15]) Ho^{3+} ions are considered to substitute for the Ti sites, even at a lower T_s Ho^{3+} ions inevitably enter the Ti sites in part, as observed in Fig. 3c. It is more expensive and complicated to detect the amount of Ho^{3+} ions dissolved in the $BaTiO_3$ lattice using an ion implantation technique with an accelerating voltage of 500 keV and secondary-ion mass spectrometry (SIMS)[11]. The PL of the $^5G_6/^5F_1 \rightarrow {}^5I_7$ transition is sensitive to Ho^{3+} on the Ti sites in $BaTiO_3$. Thus, the application of PL under 488-nm excitation may provide a probe for the occupations of Ho^{3+} ions on the Ti sites in $BaTiO_3$ ceramics co-doped with Ho^{3+} and other dopants. Accordingly, the application of PL under 532- or 638-nm excitations may provide a probe for the occupations of Ho^{3+} on the Ba site.

Conclusions

The nominal $(Ba_{1-x}Ho_x)Ti_{1-x/4}O_3$ ($x = 0.01$) (BHTH) ceramic was prepared at 1400 °C using the solid-state reaction method. BHTH exhibits a single-phase tetragonal perovskite structure. The study on the defect chemistry indicates that the defects in BHTH are Ba-site Ho^{3+} ($Ho_{Ba}^{\bullet}$), Ba vacancies (V_{Ba}''), and Ti-site Ho^{3+} (Ho_{Ti}'). The real formula of BHTH is expressed by $(Ba_{1-x}Ho_{3x/4})(Ti_{1-x/4}Ho_{x/4})O_3$. The change in local environment and crystal field at which Ho^{3+} lies plays a decisive role in photoluminescence (PL) of Ho^{3+} ions. Upon 532- and 638-nm excitations, three PL bands corresponding to $^5F_4/^5S_2 \rightarrow {}^5I_8$, $^5F_5 \rightarrow {}^5I_8$, and $^5F_4/^5S_2 \rightarrow {}^5I_7$ transitions are attributed to the contributions from Ho^{3+} ions on the Ba sites in the $BaTiO_3$ lattice. On the contrary, Ho^{3+} ions on the Ti sites are responsible for the $^5G_6/^5F_1 \rightarrow {}^5I_7$ transition under 488-nm excitation, and moreover, PL and Raman scattering can occur simultaneously as two distinct optical processes. The common Raman spectrum of $BaTiO_3$ can be observed without PL disturbance using 785-nm excitation wavelength. The PL signals under 532-nm excitation are intense enough to conceal the traditional Raman phonon modes of $BaTiO_3$. The application of PL may provide a probe for the site occupations of Ho^{3+} in $BaTiO_3$ dielectric ceramics co-doped with Ho^{3+} and other dopants.

References

1. Cao, R. *et al*. 2 μm emission properties and nonresonant energy transfer of Er^{3+} and Ho^{3+} codoped silicate glasses. *Sci. Rep.* **6**(37873), 1–11 (2016).
2. Li, G. *et al*. Diode-pumped efficient laser operation spectroscopy of Tm:Ho:YVO_4. *Opt. Mater.* **33**, 937–941 (2011).
3. Zmojda, J. *et al*. Investigation of upconversion luminescence in antimony–germanate double-clad two cores optical fiber co-doped with,Yb^{3+}/Tm^{3+} and Yb^{3+}/Ho^{3+} ions. *J. Lumin.* **170**, 795–800 (2016).
4. Mahata, M. K., Koppe, T., Kumar, K., Hofsäss, H. & Vetter, U. Demonstration of temperature dependent energy migration in dual-mode YVO_4: Ho^{3+}/Yb^{3+} nanocrystals for low temperature thermometry. *Sci. Rep.* **6**(36342), 1–11 (2016).
5. Ryba-Romanowski, W., Komar, J., Niedzwiedzki, T., Głowacki, M. & Berkowski, M. Excited state relaxation dynamics and up-conversion phenomena in $Gd_3(Al,Ga)_5O_{12}$ single crystals co-doped with holmium and ytterbium. *J. Alloys Compd.* **656**, 573–580 (2016).
6. Zhu, Y. *et al*. Broad white light and infrared emission bands in YVO_4:Yb^{3+},Ln^{3+} ($Ln^{3+} = Er^{3+}$, Tm^{3+}, or Ho^{3+}). *Appl. Phys. Express* **5**(092701), 1–3 (2012).
7. Kishi, H., Mizuno, Y. & Chazono, H. Base-metal electrode-multilayer ceramic capacitors: past, present and future perspectives. *Jpn. J. Appl. Phys.* **41**, 1–15 (2003).
8. Gong, H., Wang, X., Zhang, S. & Li, L. Synergistic effect of rare-earth elements on the dielectric properties and reliability of $BaTiO_3$-based ceramics for multilayer ceramic capacitors. *Mater. Res. Bull.* **73**, 233–239 (2016).
9. Hanafi, Z. M., Ismail, F. M., Hammad, F. F. & Nasser, S. A. Structural investigation of the phase transition in perovskite titanate containing additives. *J. Mater. Sci.* **27**, 3988–3992 (1992).
10. Makovec, D., Samardzija, Z. & Drofenik, M. Solid solubility of holmium, yttrium, dysprosium in $BaTiO_3$. *J. Am. ceram. soc.* **87**, 1324–1329 (2004).
11. Itoh, J. *et al*. Diffusion and solubility of holmium ions in barium titanate ceramics. *J. Mater. Res.* **19**, 3512–3520 (2004).
12. Jeong, J., Lee, E. J. & Han, Y. H. Electrical properties of holmium-doped $BaTiO_3$. *Jpn. J. Appl. Phys.* **44**, 4047–4051 (2005).
13. Cernea, M. *et al*. Electrical investigations of holmium-doped $BaTiO_3$ derived from sol-gel combustion. *J. Mater. Res.* **25**, 1057–1063 (2010).
14. Jeong, J., Lee, E. J. & Han, Y. H. Effects of Ho_2O_3 addition on defects of $BaTiO_3$. *Mater. Chem. Phys.* **100**, 434–437 (2006).
15. Liu, Y. & West, A. R. Ho-doped $BaTiO_3$: Polymorphism, phase equilibria and dielectric properties of $BaTi_{1-x}Ho_xO_{3-x/2}$: $0 \le x \le 0.17$. *J. Eur. Ceram. Soc.* **29**, 3249–3257 (2009).
16. Shannon, R. D. Revised effective ionic radii and systematic studies of interatomic distances in halides and chalcogenides. *Acta Crystallogr. Sect. A* **32**, 751–767 (1976).
17. Kchikech, M. & Maglione, M. Electron and lattice excitations in $BaTiO_3$-La. *J. Phys. Conden. Matt.* **6**, 10159–10170 (1994).

18. Morrison, F. D., Sinclair, D. C. & West, A. R. Electrical and structural characteristics of lanthanum-doped barium titanate ceramics. *J. App. Phys.* **86**, 6355–6366 (1999).
19. Dobal, P. S., Dixit, A. & Katiyar, R. S. Effect of lanthanum substitution on the Raman spectra of barium titanate thin films. *J. Raman Spectrosc.* **38**, 142–146 (2007).
20. Liu, Y., Feng, Y., Wu, X. & Han, X. Microwave absorption properties of La doped barium titanate in X-band. *J. Alloys Compd.* **472**, 441–445 (2009).
21. Chen, M. S. *et al*. Stress effect on Raman spectra of Ce-doped $BaTiO_3$ film. *J. Phys. Condens. Mat.* **12**, 7013–7023 (2000).
22. Lu, D. Y., Han, D. D., Sun, X. Y., Zhuang, X. L. & Zhang, Y. F. Raman evidence for Ba-site Ce^{3+} in $BaTiO_3$. *Jpn. J. Appl. Phys.* **52**(111501), 1–4 (2013).
23. Lu, D. Y., Sun, X. Y., Liu, B., Zhang, J. L. & Ogata, T. Structural and dielectric properties, electron paramagnetic resonance, and defect chemistry of Pr-doped $BaTiO_3$ ceramics. *J. Alloys Compd.* **615**, 25–34 (2014).
24. Yao, Z. *et al*. Structure and dielectric behavior of Nd-doped $BaTiO_3$ perovskites. *Mater. Chem. Phys.* **109**, 475–481 (2008).
25. Lu, D. Y. *et al*. Self-compensation characteristics of Eu ions in $BaTiO_3$. *Solid State Ionics* **201**, 6–10 (2011).
26. Lu, D. Y. Self-adjustable site occupations between Ba-site Tb^{3+} and Ti-site Tb^{4+} ions in terbium-doped barium titanate ceramics. *Solid State Ionics* **276**, 98–106 (2015).
27. Lu, D. Y. & Cui, S. Z. Defects characterisation of Dy-doped $BaTiO_3$ ceramics via electron paramagnetic resonance. *J. Eur. Ceram. Soc.* **34**, 2217–2227 (2014).
28. Lu, D. Y. *et al*. Abnormal Raman spectra in Er-doped $BaTiO_3$ ceramics. *J. Raman Spectrosc.* **45**, 963–970 (2014).
29. Amami, J. *et al*. Second harmonic generation and Yb^{3+} cooperative emission used as structural probes in size-driven cubic-tetragonal phase transition in $BaTiO_3$ sol–gel nanocrystals. *J. Lumin.* **119–120**, 383–387 (2006).
30. Ganguly, M., Rout, S. K., Ahn, C. W., Kim, I. W. & Kar, M. Structural, electrical and optical properties of $Ba(Ti_{1-x}Yb_{4x/3})O_3$ ceramics. *Ceram. Int.* **39**, 9511–9524 (2013).
31. Kumar, G. A., Martinez, A., Mejia, E. & Eden, J. G. Fluorescence and upconversion spectral studies of Ho^{3+} in alkali bismuth gallate glasses. *J. Alloys Compd.* **365**, 117–120 (2004).
32. Babu, S., Seshadri, M., Balakrishna, A., Reddy Prasad, V. & Ratnakaram, Y. C. Study of multicomponent fluoro-phosphate based glasses: Ho^{3+} as a luminescence center. *Physica B* **479**, 26–34 (2015).
33. Pandey, A. & Swart, H. C. Luminescence investigation of visible light emitting Ho^{3+} doped tellurite glass. *J. Lumin.* **169**, 93–98 (2016).
34. Valiev, U. V. *et al*. Study of the line intensity in the optical and magnetooptical spectra in holmium-containing paramagnetic garnets. *Opt. Mater.* **51**, 42–49 (2016).
35. Battisha, I. K. Visible up-conversion luminescence in Ho^{3+}: $BaTiO_3$ nano-crystals prepared by sol gel technique. *J. Sol-Gel Sci. Techn.* **30**, 163–172 (2004).
36. Secu, M., Cernea, M., Secu, C. E. & Vasile, B. S. Structural characterization and photoluminescence of nanocrystalline Ho-doped $BaTiO_3$ derived from sol–gel method. *J. Nanopart. Res.* **13**, 3123–3128 (2011).
37. Kolodiazhnyi, T. & Petric, A. Analysis of point defects in polycrystalline $BaTiO_3$ by electron paramagnetic resonance. *J Phys Chem Solids* **64**, 953–960 (2003).
38. Dunber, T. D., Warren, W. L., Tuttle, B. A., Randall, C. A. & Tsur, T. Electron paramagnetic resonance investigation of lanthanide-doped barium titanate: dopant site occupancy. *J. Phys. Chem. B* **108**, 908–917 (2004).
39. Kröger, F. A. & Vink, H. J. *Solid State Physics III* (Academic Press, New York, 1956).
40. DrDomenico, M., Wemple, J. S. H., Porto, S. P. S. & Rauman, R. P. Raman spectrum of single-domain $BaTiO_3$. *Phys. Rev.* **174**, 522–530 (1968).
41. Gupta, S. Investigations of micro-stress and phase transition in so-gel-derived multideposited coatings of barium titanate using Raman spectroscopy. *J. Raman Spectrosc.* **33**, 42–49 (2002).
42. Buscaglia, V. *et al*. Raman and AFM piezoresponse study of dense $BaTiO_3$ nanocrystalline ceramics. *J. Eur. Ceram. Soc.* **25**, 3059–3062 (2005).
43. Gajović, A., Tomašić, N., Djerdj, I., Su, D. S. & Furić, K. Influence of mechanochemical processing to luminescence properties in Y_2O_3 powder. *J. Alloys Compd.* **456**, 313–319 (2008).
44. Lu, D. Y. & Liu, T. T. Dielectric properties and defect chemistry of $(Ba_{1-x}La_x)(Ti_{1-x}Lu_x)O_3$ ceramics. *J. Alloys Compd.* **698**, 967–976 (2017).
45. Ikushima, H. & Mayakawa, S. Electron spin resonance Mn^{2+} in $BaTiO_3$. *J. Phys. Soc. Jpn.* **19**, 1986 (1964).
46. Müller, K. A., Berlinger, W., Blazey, K. W. & Albers, J. Electron paramagnetic resonance of Mn^{4+} in $BaTiO_3$. *Solid State Commun.* **61**, 21–25 (1987).
47. Kishi, H. *et al*. The effect of rare-earth (La, Sm, Dy, Ho and Er) and Mg on the microstructure in $BaTiO_3$. *J. Eur. Ceram. Soc.* **19**, 1043–1046 (1999).
48. Jeong, J., Lee, E. J. & Han, Y. H. Defect chemistry and electrical degradation of $BaTiO_3$ co-doped with Ho and Mn. *J. Eur. Ceram. Soc.* **27**, 1159–1163 (2007).
49. Sagar, R., Hudge, P., Madolappa, S., Kumbharkhane, A. C. & Raibagkar, R. L. Electrical properties and microwave dielectric behavior of holmium substituted barium zirconium titanate ceramics. *J. Alloys Compd.* **537**, 197–202 (2012).
50. Jha, P. A. & Jha, A. K. Effect of holmium substitution on structural and electrical properties of barium zirconate titanate ferroelectric ceramics. *Ceram. Int.* **40**, 5209–5216 (2014).

Acknowledgements

This work was supported by the projects of the National Natural Science Foundations of China (Grant No. 21271084) and of Jilin Province (20160101290JC), and Changbai Mountain Scholar Distinguished Professor (2015047). The authors would like to thank Dr. Zhenyu Liu in The Hong Kong Polytechnic University for the help of photoluminescence analyses.

Author Contributions

D.X.G. conducted the synthesis, XRD, SEM, EPR, Raman, and PL measurements of Ho-doped $BaTiO_3$ ceramics. D.Y.L. supervised the work, carried out the analysis of all the data, and wrote the main manuscript text. All authors reviewed the manuscript.

Additional Information

Competing Interests: The authors declare that they have no competing interests.

Publisher's note: Springer Nature remains neutral with regard to jurisdictional claims in published maps and institutional affiliations.